iScience, Volume *24*

Supplemental information

Coevolutionary transitions emerging from flexible molecular recognition and eco-evolutionary feedback

Jiming Sheng and Shenshen Wang

Table S1: Simulation parameters, related to Figure 3

Parameter	Notation	Value
Number of shape-space dimensions	n	8
Number of variable dimensions	n_v	4–6
Number of conserved dimensions	n_c	4–2
Number of dimensions of BCR-Ag binding footprint	n_b	3
Maximum B cell affinity to the founder virus ($k_{\mathrm{B}}T$)	A_{max}	8
Radius of B cell founder hypersphere	R_f	4.9
Average affinity advantage of germline B cells' optimal footprint over other footprints ($k_{\mathrm{B}}T$)	λ	2
B cell carrying capacity	K_b	10^6
Total number of distinct germline B cells		5000
Total number of FDC Ag	$K_{a,GC}$	10^5
Number of FDC Ags each B cell encounters in a GC cycle		100
Fraction of GC B cells receiving T cell help	f_{Tfh}	0.7
Probability of differentiation into memory cells	p_{mem}	0.05
Probability of differentiation into plasma cells	p_{pla}	0.05
Affinity threshold for plasma cell differentiation ($k_{\mathrm{B}}T$)	A_{pla}	5
Probability of mutation in each daughter B cell	μ_B	0.5
Fraction of lethal BCR mutation	p_{let}	0.3
Fraction of affinity-altering BCR mutation	p_{aa}	0.2
Fraction of silent BCR mutation	p_{sil}	0.5
Average B cell mutation step size in variable dimensions	$\Delta_{B,v}$	2
Average B cell mutation step size in conserved dimensions	$\Delta_{B,c}$	1
Initial size and capacity of Ag population	K_a	10^5
Initial Ag diversity	σ_A	0–2
Number of plasma cells each Ag encounters in each cycle		100
Probability of mutation per Ag per generation	μ_{Ag}	$0.01n_v/4$
Average Ag mutation step size in variable dimensions	Δ_A	2
Extinction threshold of Ag population		100
Total number of GCs		$1, 10, 100$
Concentration coefficient of FDC Ag	$C_{Ag,0}$	0.05
Concentration coefficient of Plasma BCR	$C_{Pla,0}$	0.005
Simulation time span (GC cycle)	T_{max}	200
Affinity threshold of bnAbs ($k_{\mathrm{B}}T$)		6

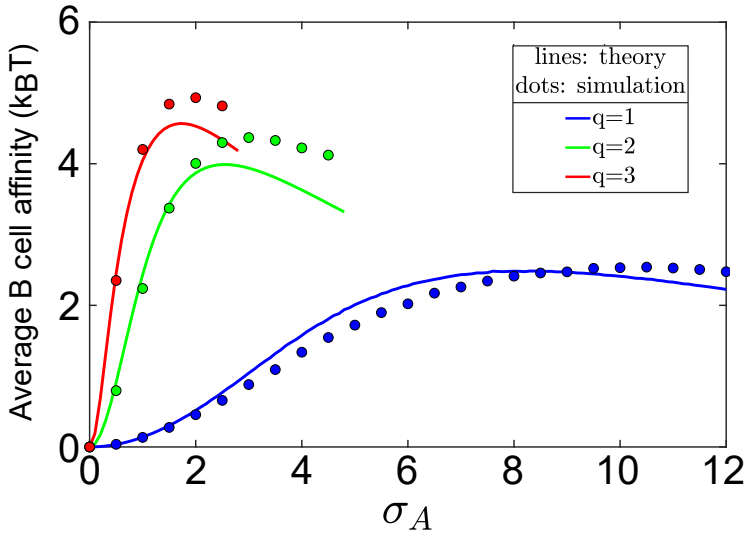

Figure S1: **Average binding affinity of founder B cells to initial antigens increases with antigen diversity (σ_A) when diversity is modest. Related to Figure 4.** Curves, as given by Eqs.18, 21, terminate when σ_A reaches the radius of the founder hypersphere, $R_f = (n_b A_{max})^{1/q}$. Good agreement with simulations (symbols) is achieved, even at moderately large σ_A. Here, $n_b = 3$ and $A_{max} = 8$.

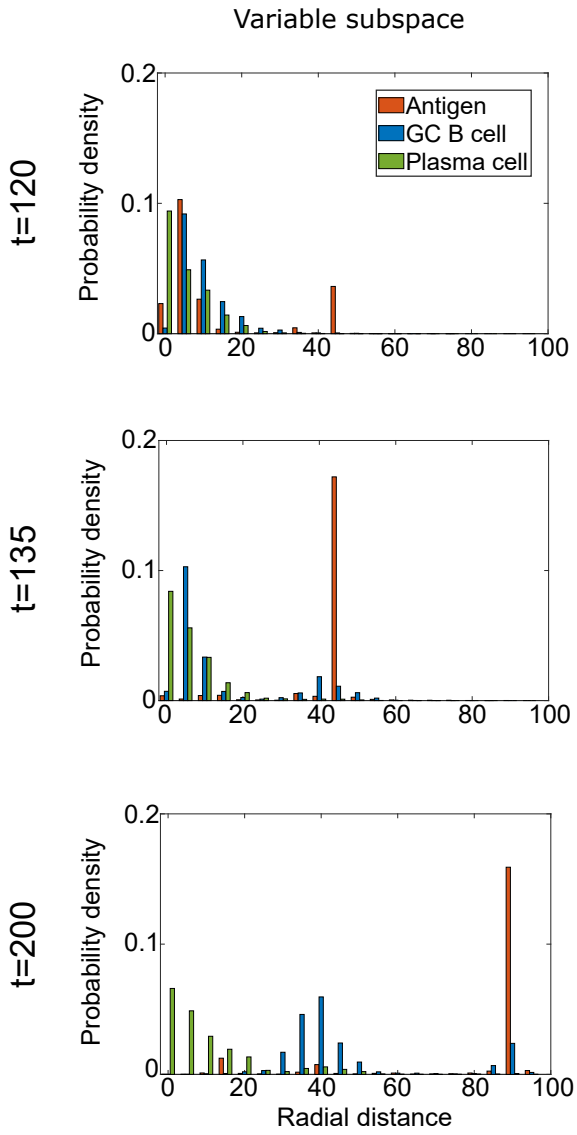

Figure S2: **Radial distribution of antigens, GC B cells and plasma cells in the persistence phase. Related to Figure 3.** Driven by strain-specific GC B cells (blue), mutant antigens (red) emerge increasingly farther from the founder strain at the origin that focuses plasma cells (green). Data are collected from the same simulation as shown in Fig. 3D, at time points marked therein and in the same subspace as in Fig. 3G. Radial distance is measured by r^2/n_b, where r is the Euclidean distance between an agent and the subspace origin; $n_b = 3$ is the dimensionality of binding subspace. $n_c = 2$, $\sigma_A = 0.5$. The same legend applies to all panels.

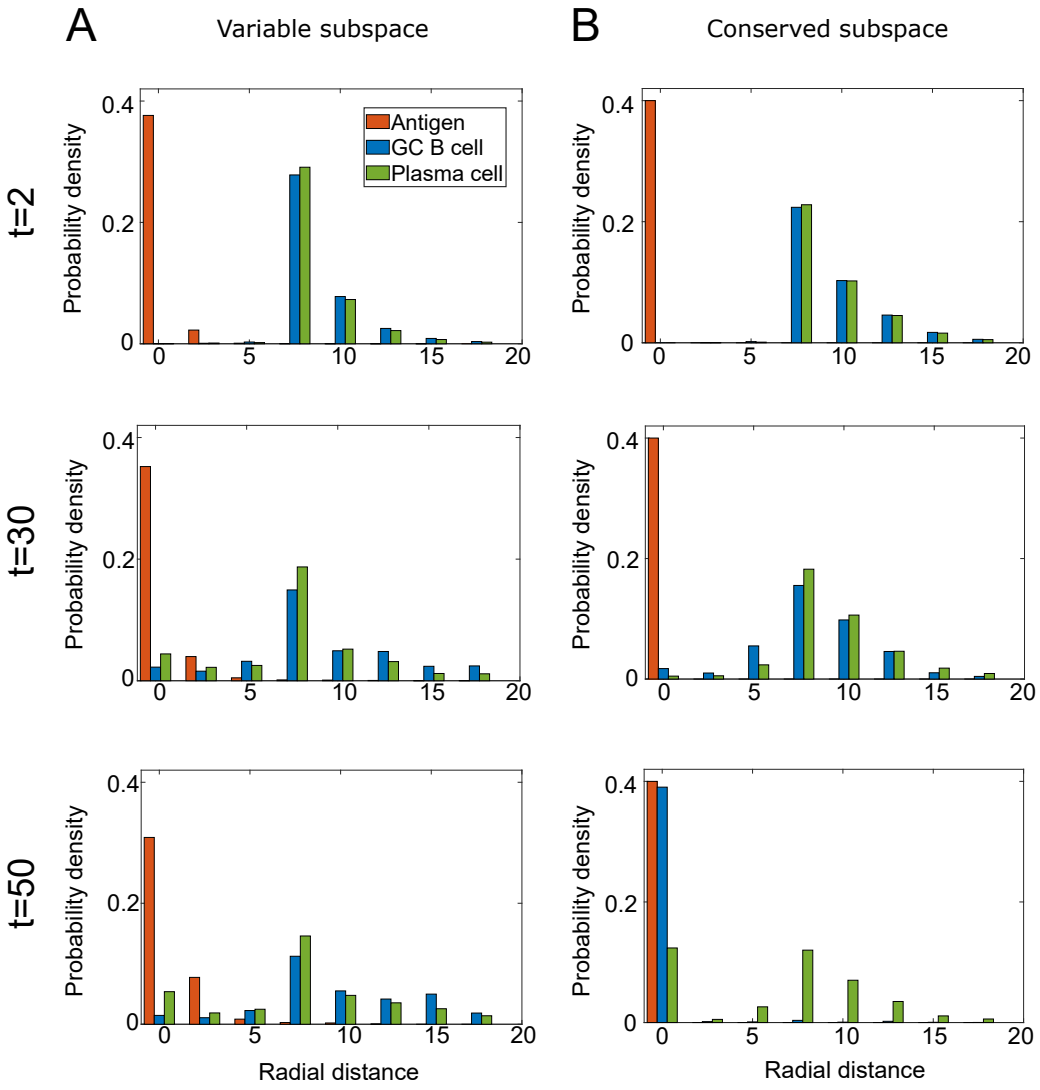

Figure S3: **Radial distribution of antigens, GC B cells and plasma cells in the clearance phase. Related to Figure 3.** Rapid convergence of GC B cells (blue) toward the origin in the conserved subspace leads to clearance of antigen (red) soon afterward. Note that the plasma cell distribution develops a peak at the origin of the conserved subspace (B) while remaining similar in the variable subspace (A) at later times. From the same simulation as in Fig. 3F at marked time points and in the same conserved subspace as in Fig. 3I. (A)/(B): Radial distribution in a fully variable/conserved subspace. $n_c = 3$, $\sigma_A = 1$. The same legend applies to all panels.

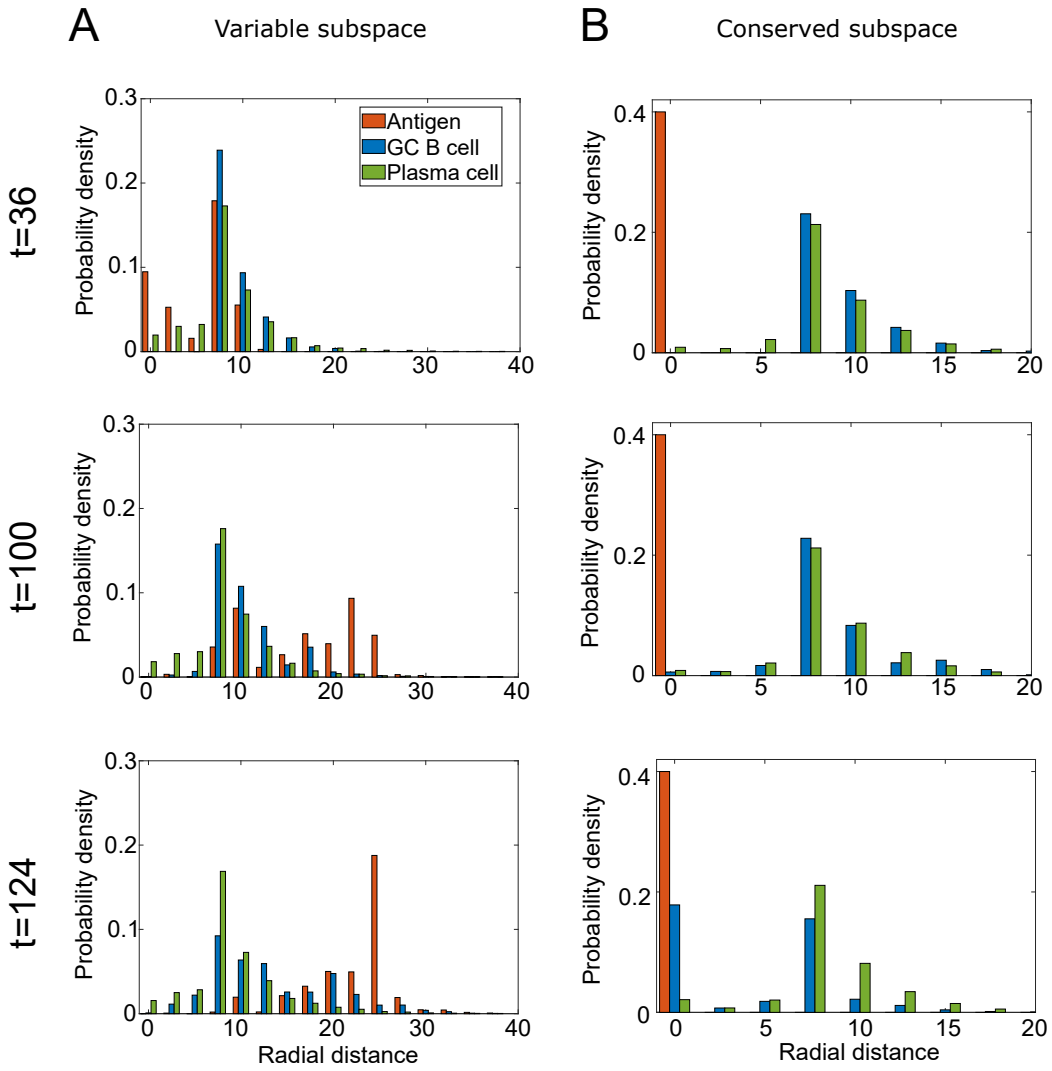

Figure S4: **Radial distribution of antigens, GC B cells and plasma cells in the rebound phase. Related to Figure 3.** Antigen population goes through the bottleneck ($t = 36$), recovers to a high level ($t = 100$), and finally declines toward extinction ($t = 124$). Antigens (red) are capable of evading elimination by GC B cells (blue) in the variable subspace (panel A) but remaining at the origin in the conserved subspace (panel B); the distribution of plasma cells (green) has hardly changed in the variable subspace over this course. Same simulation as that shown in Fig. 3E and the same variable subspace as that in Fig. 3H. $n_c = 3$, $\sigma_A = 2$. The same legend applies to all panels.

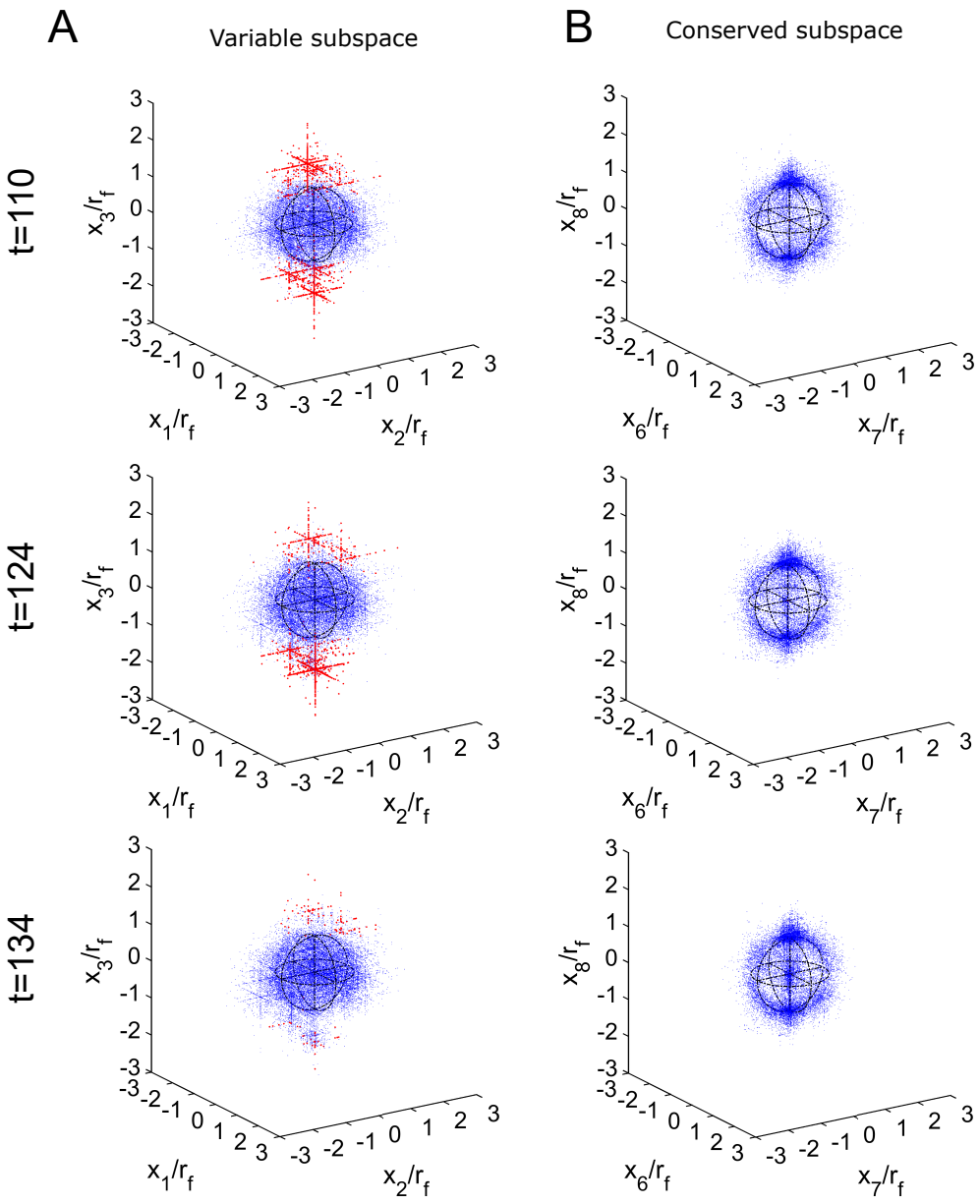

Figure S5: **Shape-space snapshots in the rebound phase, after recovering from population bottleneck. Related to Figure 3.** Antigens are eventually cleared as newly generated plasma cells converge to the origin in the conserved subspace. Data are collected from the same simulations as those in Figs. 3E and 3H. Panel A/B: configurations of antigens (red) and plasma cells (blue) in a fully variable/conserved subspace. Top row: at $t = 110$, antigen population peaks following recovery from the bottleneck; middle: at $t = 124$, antigen population just falls below %50 of the peak value; bottom: antigens are close to extinction. Here $n_c = 3$, $\sigma_A = 2$.

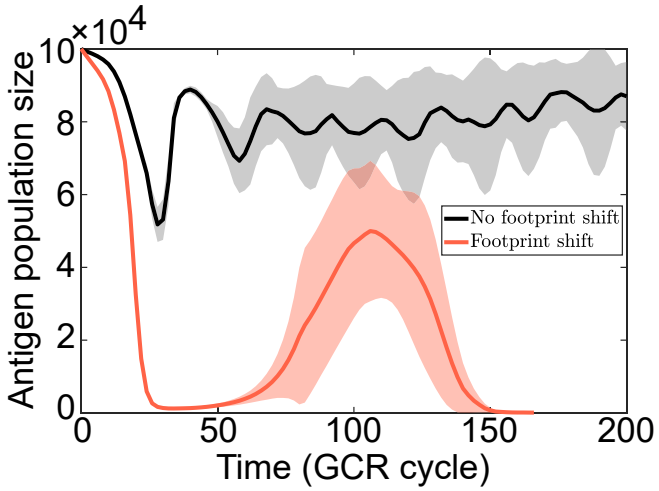

Figure S6: **Antigen population trajectories in the rebound phase in the presence and absence of footprint shift. Related to Figure 6.** Without footprint shift, antigen removal by plasma cells becomes ineffective, resulting in viral persistence instead. Each curve depicts mean±SD over 5 simulations. $n_c = 4, \sigma_A = 2$.

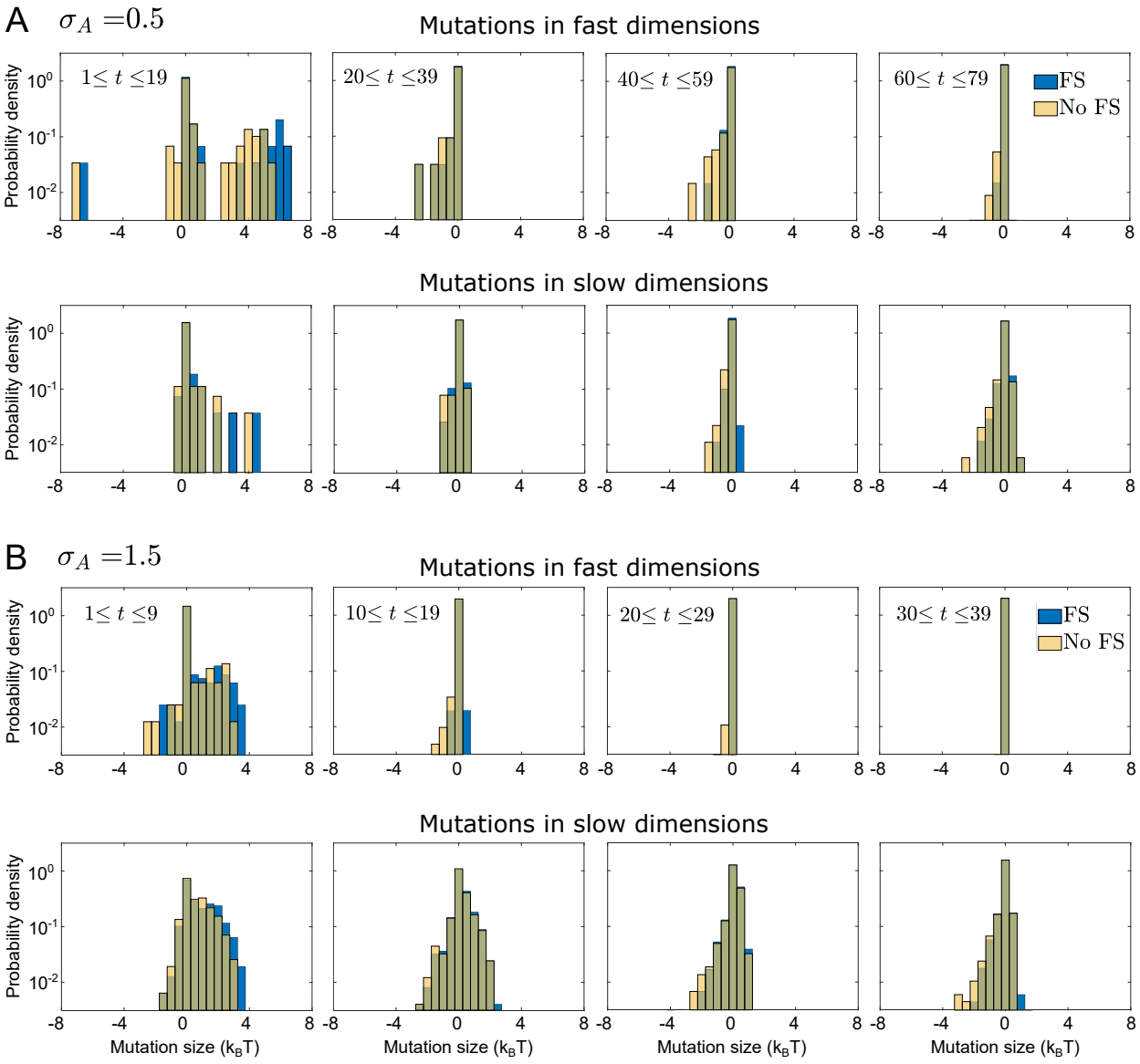

Figure S7: **Time-dependent distribution of mutation effect in fast (variable) and slow (conserved) dimensions. Related to Figures 7 and 8.** Beneficial BCR mutations remain available in slow dimensions but are quickly depleted in fast dimensions. Mutation size is measured by the difference in log-mean-exponential affinity of a B cell to its encountered FDC antigens before and after a mutation (see Section 2.7); a positive value indicates a beneficial mutation. In the case of a fixed footprint ("No FS", yellow), binding footprint is unchanged following a mutation regardless of its potential effect. Affinity-optimizing footprint shift enables the usage of mutations outside current contact and augments the beneficial effect ("FS", blue). Data are collected from long-lived lineages descending from B-type founders in repeated simulations, like in Fig. 8. Here, $n_c = 4$, $\sigma_A = 0.5$ in (A) and $\sigma_A = 1.5$ in (B). The same color scheme applies to all panels.

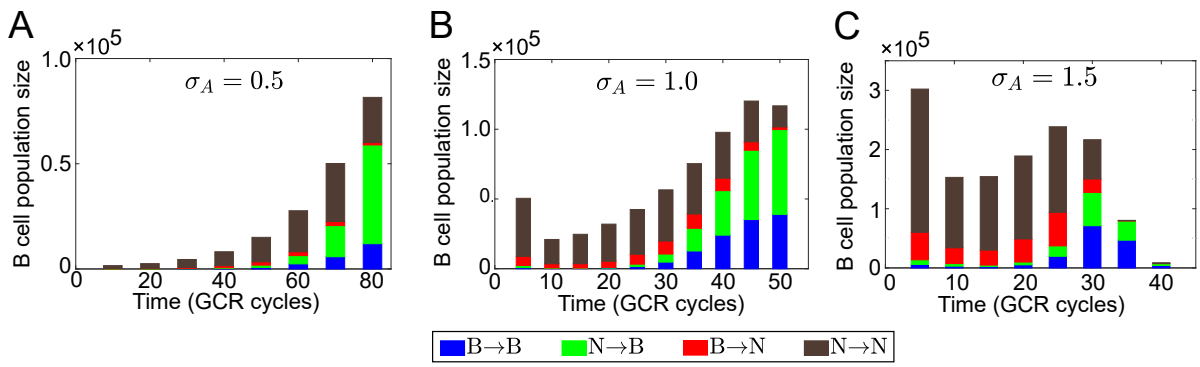

Figure S8: **Time evolution of absolute B cell count in each of four types of identity switch. Related to Figure 7.** Switch types are defined based on the initial and current identity of individual cells, e.g. N→B represents current B-type clones descending from an N-type germline ancestor. From the same simulations in Fig. 7B. $n_c = 4$ in all panels.

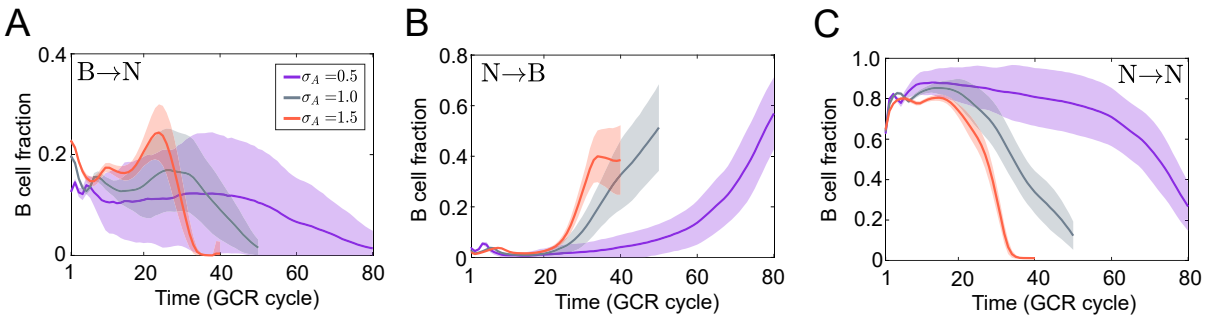

Figure S9: **Prevalence of B cells taking B→N, N→B and N→N pathways of identity switch. Related to Figure 7.** From the same simulations as in Fig. 7. $n_c = 4$. Data are plotted as mean ±SD and the same color scheme applies to all panels.

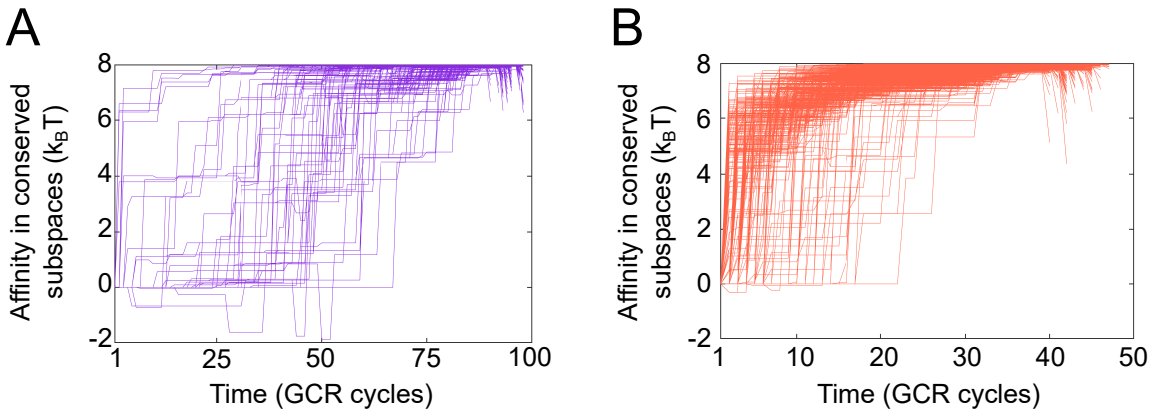

Figure S10: **Binding affinity to conserved targets along the B→B lineages. Related to Figure 8.** (A) A modest initial antigen diversity ($\sigma_A = 0.5$) prolongs affinity maturation and permits a wide range of paths (tolerating occasional deleterious mutations). (B) A high initial antigen diversity ($\sigma_A = 1.5$) hastens maturation and yields a strong selection pressure that narrows the viable paths. Each trajectory represents a single line of B cells that both starts and ends as B-type. Data are from the same simulations as in Figs. 8G and 8H. $n_c = 4$.

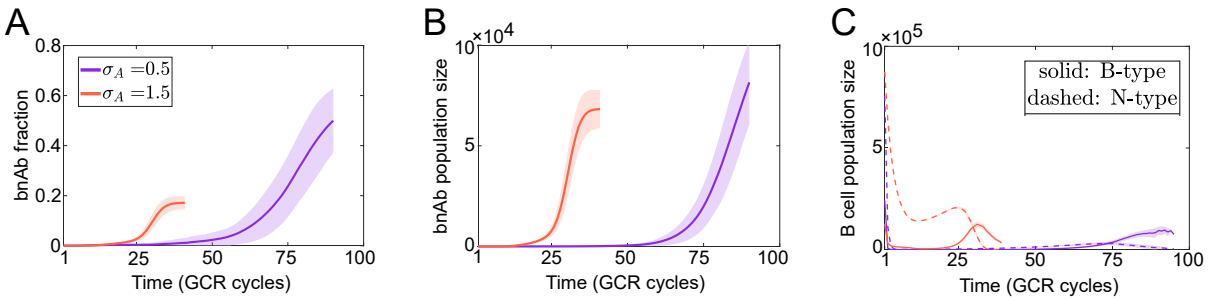

Figure S11: **Increasing initial antigen diversity speeds up accumulation of bnAbs and recovery of B-type cells, at the expense of hastened affinity maturation and reduced bnAb prevalence upon clearance. Related to Figure 8.** Affinity threshold of bnAbs (binding fully conserved targets) is set to $6k_BT$. From the same simulations in Fig. 8C. $n_c = 4$. Data are plotted as mean±SD and the same color scheme applies to all panels.

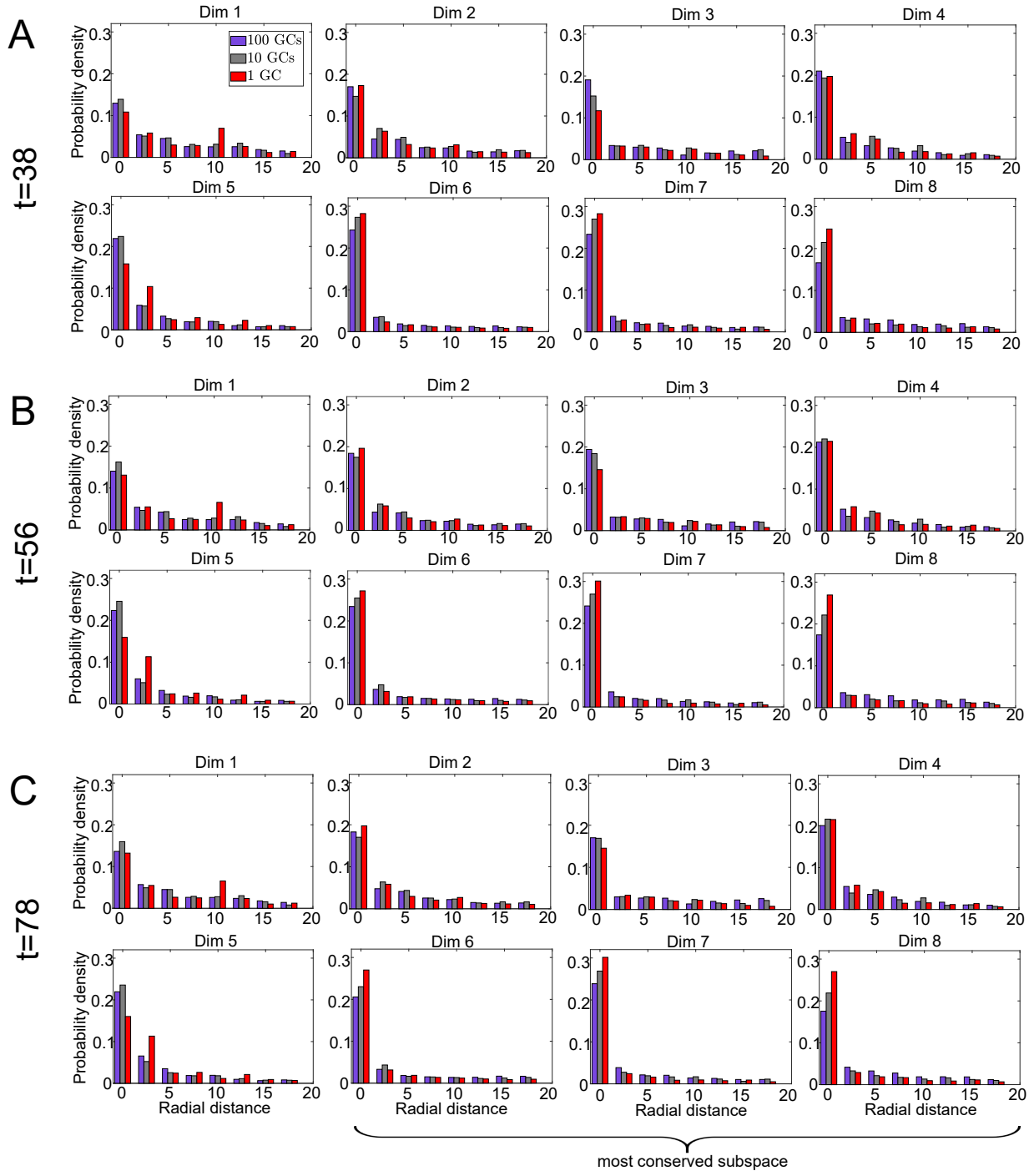

Figure S12: **Radial distribution of plasma cells during antigen population bottleneck at different levels of GC compartmentalization. Related to Figure 9.** For fewer larger GCs (purple to red), plasma cells are more concentrated toward the origin of the most conserved subspace (dimension 6 to 8). Data are taken from the same simulations as in Fig. 9B; time points are at the beginning (A), the lowest point (B), and the recovery stage (C) of the antigen population bottleneck, defined as when population size falls below 10% capacity, reaches the minimum, and rises above 50% capacity, respectively, for one GC. Radial distance in dimension k is measured by x_k^2 for each plasma cell $\vec{x}$. $n_c = 2$, $\sigma_A = 1$. The same legend applies to all panels.

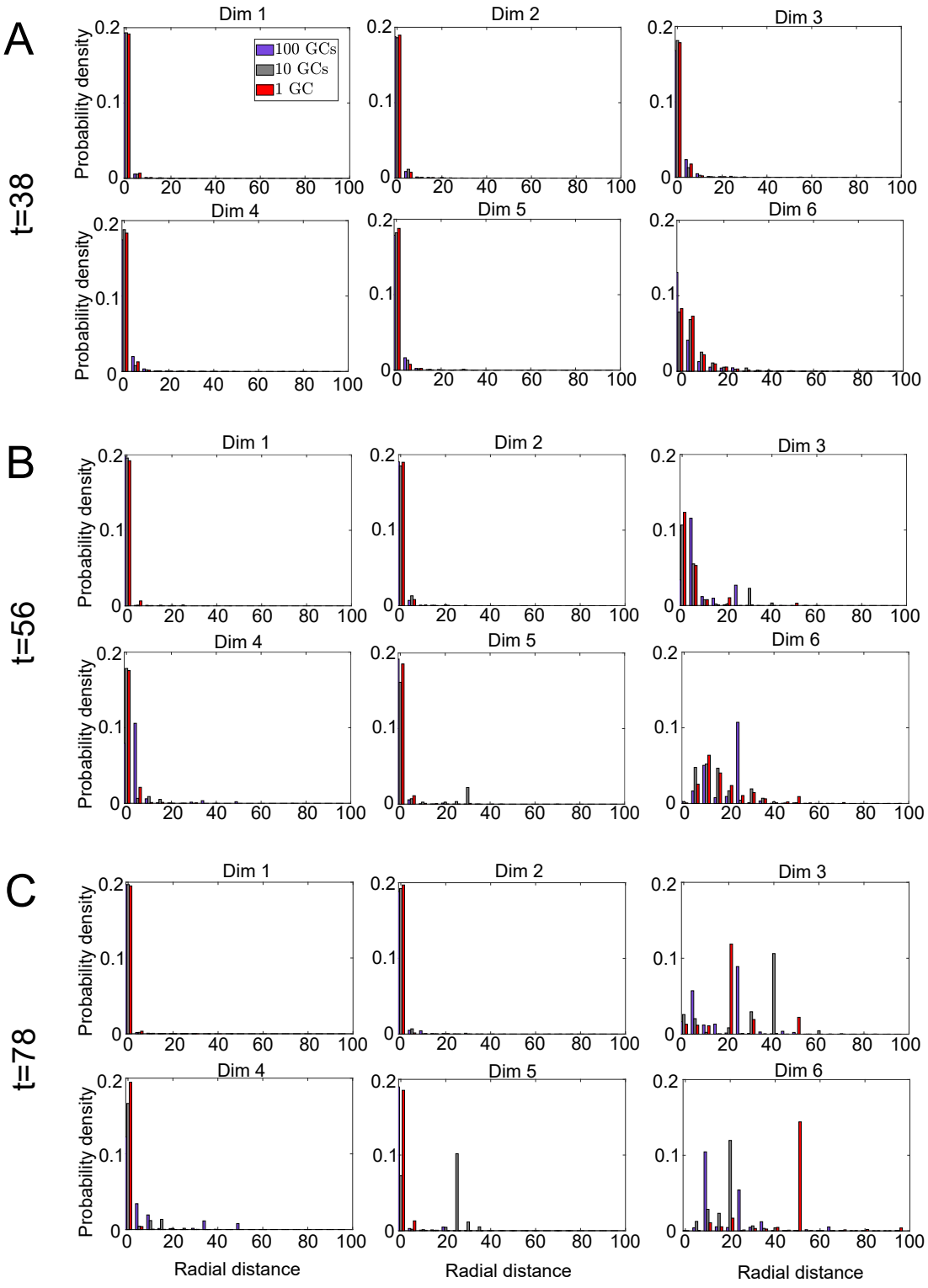

Figure S13: **Radial distribution of antigens during population bottleneck at different levels of GC compartmentalization. Related to Figure 9.** For fewer larger GCs (purple to red), antigens are driven farther away from the origin in the variable dimension (dimension 6) of the most conserved subspace (dimension 6 to 8) during recovery from the population bottleneck. Data are taken from the same simulations as in Fig. 9B; time points in A to C are chosen like in Fig.S12. Radial distance in dimension k is measured by y_k^2 for each circulating antigen $\vec{y}$. $n_c = 2$, $\sigma_A = 1$. The same legend applies to all panels.

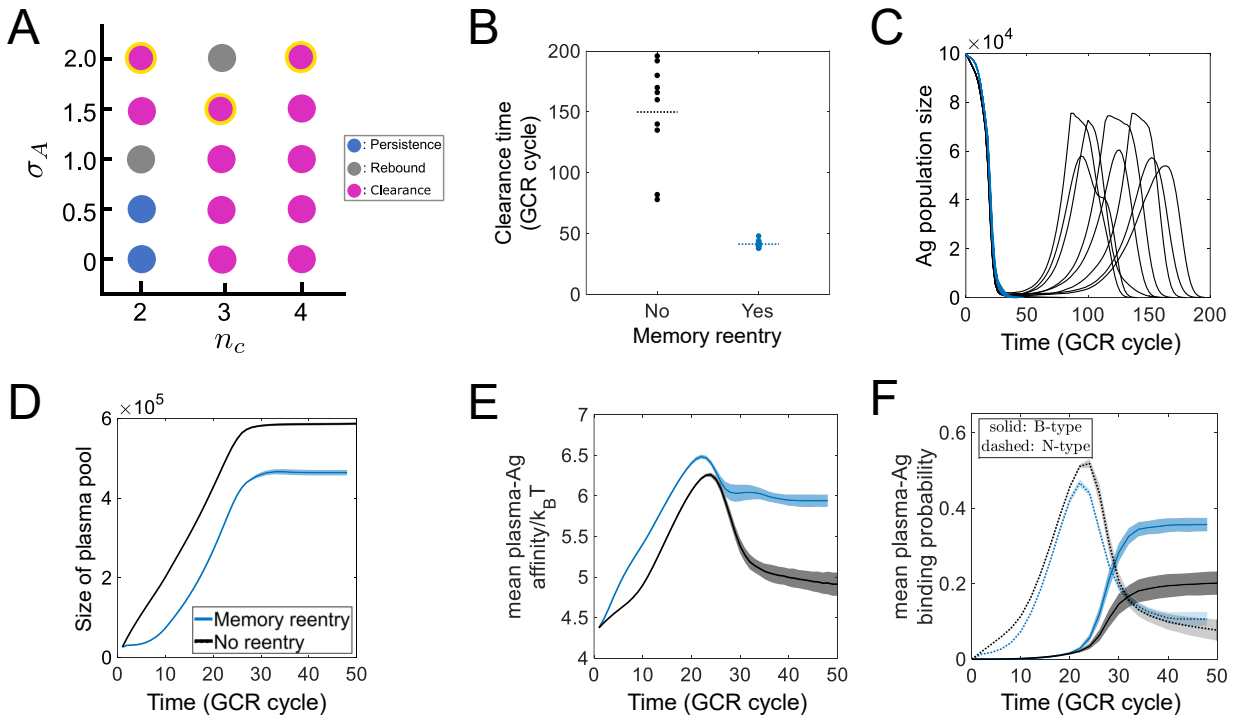

Figure S14: **Memory reentry into ongoing GCs promotes broad antibody response and turns viral rebound into rapid clearance. Related to Figure 3.** (A) Coevolutionary outcomes with memory reentry. Yellow outlines highlight changes compared to Fig. 3A; memory reentry turns mixed outcomes into rapid clearance. (B) Time until viral clearance. Each symbol is an independent simulation; dashed lines indicate the mean values. (C) Ag population trajectories. Each curve is one simulation. (D), (E) Overall quantity (D) and quality (E) of antibody-secreting cells (including both plasma and memory cells). (F) Efficacy of antibody response, measured by plasma-Ag binding probabilities P_B and P_N (see main text for definition) for broad (B-type) and narrow (N-type) antibodies, respectively. In (B)–(F), blue (black) indicates with (without) memory reentry. Data are collected from 10 simulations each and are plotted as mean ± D in (D)–(F). Maximum memory reentry ($\alpha = 1$) in all panels. $n_c = 4$, $\sigma_A = 2$.

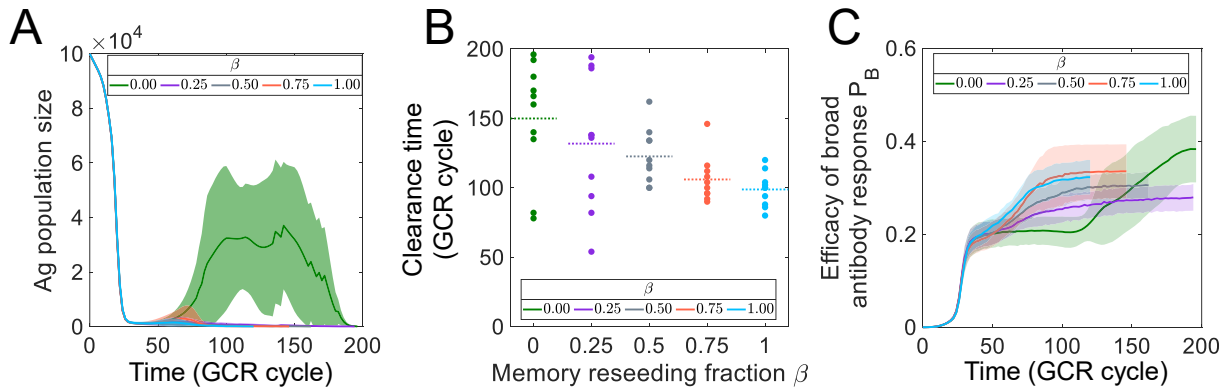

Figure S15: **Memory reseeding of new GCs results in faster development of broad antibody response and reduced viral rebound. Related to Figure 3.** A higher fraction β of memory cells among GC founders leads to (A) a reduced peak height or even prevention of Ag rebound and (B) an earlier clearance (dashed lines indicating mean clearance times), due to (C) faster development of broad antibody response (efficacy being measured by plasma-Ag binding probability P_B as defined in the main text). As the memory fraction β of new GC founders increases from 0 to 1, the fraction of trajectories along which, following the initial drop, the viral load remains below 10% of the initial level increases from 20% to 100%. Data from 10 simulations are plotted as mean±SD in (A) and (C) and with symbols in (B). $n_c = 4$, $\sigma_A = 2$.

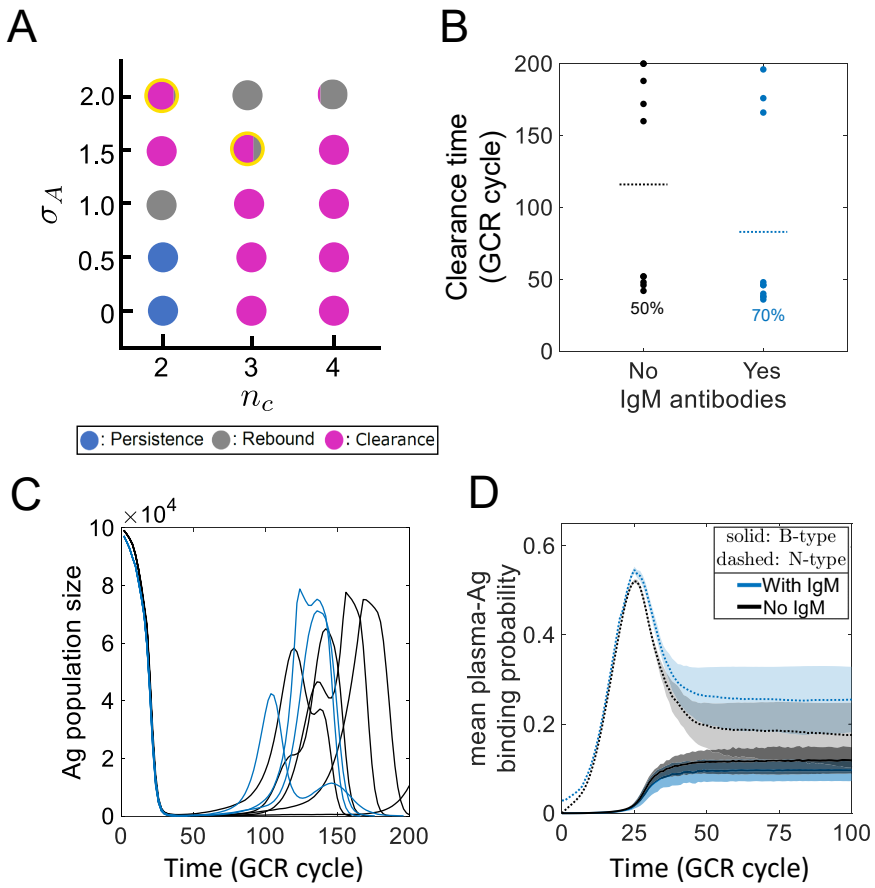

Figure S16: **IgM antibodies facilitate viral clearance by enhancing early removal and corralling escape mutants. Related to Figure 3.** (A) Phase diagram of co-evolutionary outcomes in the presence of IgM antibodies. Yellow outlines highlight an increased likelihood of clearance compared to without IgM antibodies (see Fig.3A). (B) Time to viral clearance is, on average, reduced by IgM antibodies, through a larger fraction of monotonic clearance (percentage indicated). Horizontal dashed lines mark the mean value over 10 simulations (symbols). (C) Ag population trajectories. (D) Plasma-Ag binding probabilities of broad (P_B) and specific (P_N) antibodies; data from 10 simulations are plotted as mean±SD. The same color scheme applies to (B)-(D). n_c=3, $\sigma_A = 1.5$.

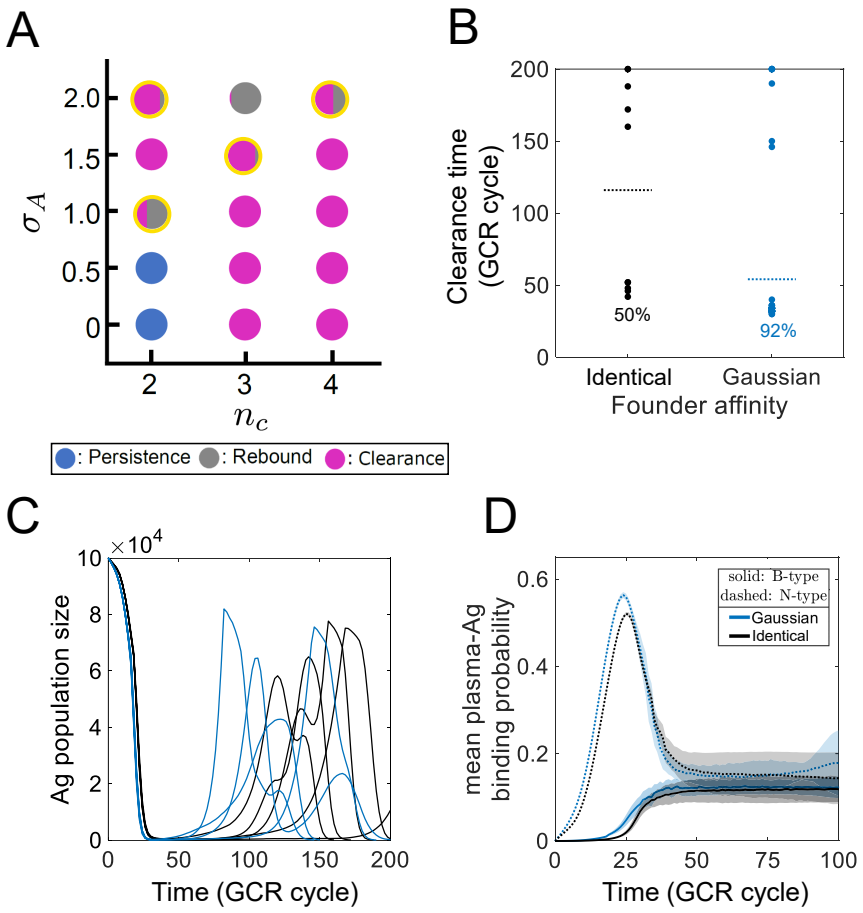

Figure S17: **A wider range of founder affinity promotes the development of both broad and specific responses and, in turn, enhances viral clearance. Related to Figure 3.** (A) Phase diagram of co-evolutionary outcomes with Gaussian-distributed founder affinities. Yellow outlines highlight a larger fraction of clearance against rebound compared to having an identical founder affinity (see Fig. 3A). (B) The time to viral clearance becomes shorter when allowing a wider range of founder affinities, mainly through a larger fraction of monotonic clearance (percentage indicated). Horizontal dashed lines mark the mean clearance times over 50 simulations. (C) Ag population trajectories. 10 out of 50 simulations are plotted for clarity. (D) Efficacy of both narrow and broad antibody responses, measured by plasma-Ag binding probabilities, P_N and P_B, respectively, rises earlier with Gaussian-distributed founder affinities, since the best clones available are preferentially expanded. Data from 50 simulations are plotted as mean±SD. The same color scheme applies to (B)-(D). n_c=3, $\sigma_A = 1.5$.

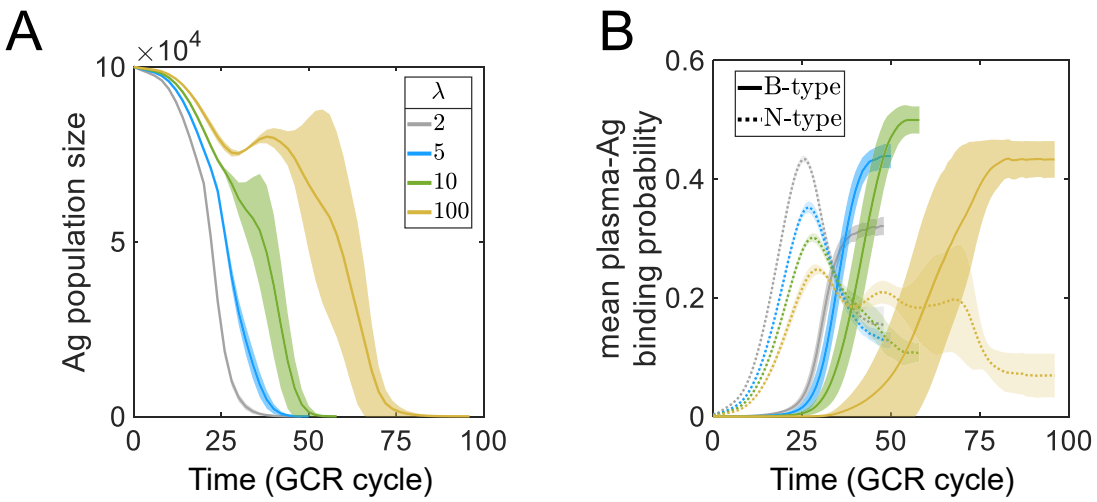

Figure S18: **Higher germline quality against the founder virus at non-optimal binding sites (smaller λ) promotes both specific and broad antibody responses and accelerates viral clearance. Related to Figures 3 and 4.** (A), (B) Time trajectories of Ag population size and plasma-Ag binding probabilities of broad (P_B) and specific (P_N) antibodies at varying λ. Smaller λ yields a stronger benefit of footprint shift and, in turn, stronger specific response and faster rising broad response. Data from 10 simulations are plotted as mean±SD. The same color scheme applies to both panels. $n_c = 4$, $\sigma_A = 1.5$. For all the results presented in the main text, $\lambda = 2$.